Journal of Applied Polymer Science

Investigation on static and dynamic performance of a hinge configuration with integrated dielectric elastomers

Chi Zhang,[1,2] Hualing Chen,[1,2] Bo Li,[1,2] Yanjie Wang,[1,2] Lei Liu,[1,2] Dichen Li[1,3]

[1]School of Mechanical Engineering, Xi'an Jiaotong University, Xi'an 710049, People's Republic of China

[2]State Key Laboratory for Strength and Vibration of Mechanical Structures, Xi'an Jiaotong University, Xi'an 710049, People's Republic of China

[3]State Key Laboratory for Manufacturing Systems Engineering, Xi'an Jiaotong University, Xi'an 710049, People's Republic of China

Correspondence to: H. Chen (E-mail: hlchen@mail.xjtu.edu.cn)

ABSTRACT: A rigid hinge frame combined with pre-stretched dielectric elastomer (DE) films can form an active biological agonist–antagonist configuration. In this structure, the DE films undergo a constant deformation under a static voltage as well as specific reciprocating rotation under an alternative voltage. To theoretically investigate the static and dynamic performance, we establish the kinetic equation of the active hinge configuration. The computational static rotary angle exhibits a good fit with the experimental data from literature. Based on this model, static performance of this configuration when DE undergoes uniaxial and pure shear deformation is investigated. Subject to a small perturbation, the configuration may oscillate around the equilibrium state and the natural frequency can be obtained. By varying the pre-stretch ratios, applied voltage, layer number, and the rotational inertia of the hinge, we can tune the natural frequency at a wide range. When the voltage is sinusoidal and varies continuously, the configuration resonates at multiple frequencies of excitation, known as harmonic and superharmonic resonance. Our research may serve as a guide to optimal design and provide insights into the performance of the hinge configuration, which can effectively expand the structure's application fields. © 2014 Wiley Periodicals, Inc. J. Appl. Polym. Sci. **2015**, *132*, 41630.

KEYWORDS: dielectric elastomer; hinge configuration; modeling; dynamics

Received 27 April 2014; accepted 12 October 2014
DOI: 10.1002/app.41630

INTRODUCTION

As a sub-category of electro-active polymers, dielectric elastomers (DE) are regarded as promising candidates for artificial muscles with the unique properties of light weight, fast response, large strain, high-energy density, and high efficiency.[1,2] A dielectric elastomer actuator is normally composed of an insulating elastomeric membrane, sandwiched between compliant electrodes, as a parallel capacitor.[3] Subject to an external voltage, the elastomer is squeezed by a compressive stress and accordingly reduces its thickness while expands in area. The compressive stress is defined as Maxwell stress, generated by the attraction of charges accumulated on the surfaces of the DE.[4] The electrical excited deformation is similar to biological muscles and explored in many applications, such as soft robots,[5] optics lens,[6,7] Braille displays,[1] electric generators,[8] spring-rolled actuators,[9–11] and agonist–antagonist configurations.[12–14]

The agonist–antagonist configuration has attracted academic interests in recent years because it offers a tunable resonator and bio-inspired applications.[15,16] Lochmatter *et al.* first presented the basic working principle of the active hinge configuration and conducted mechanical performance test, including rotary angle, blocking moment, and durability, which proved the feasibility and potential of this structure.[14,17] Jordi *et al.* studied the mechanical performance of the configuration integrated with three different materials, among which VHB shows the best actuation performance.[18] In her further study, she designed and manufactured a pisciform airship based on the active hinge configuration, verifying the structure's potential of being used in aerodynamics.[19] However, the previous studies are mainly focused on the configuration's static mechanical performance by experiment. Theoretical analysis is lacking which makes the disciplines and factors influencing the configuration's static performance cannot be mastered well. Furthermore, both of theoretical and experimental dynamic studies are vacant, considerably limiting the configuration's application in dynamic field.

In practice, the hinge configuration is mostly subject to dynamic excitation with a wide range of frequencies when

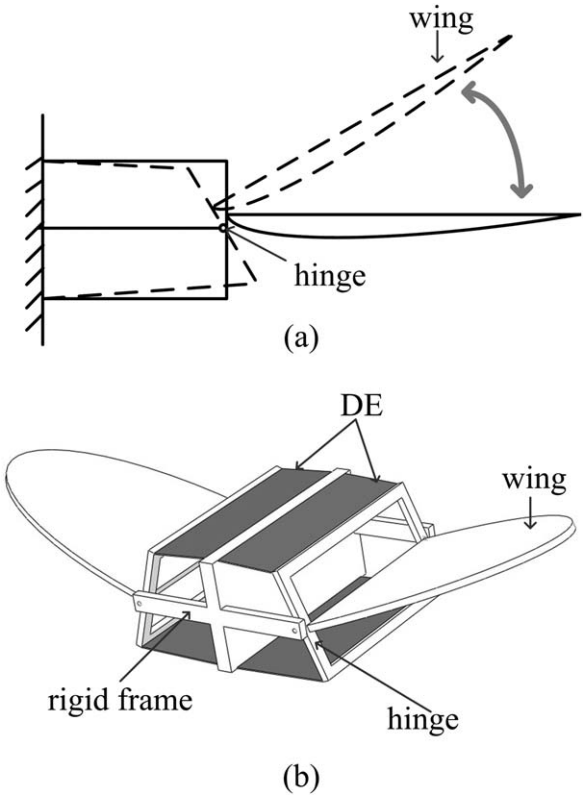

Figure 1. Conceptual design of a flapping bionics aerocraft drived by the hinge configuration with integrated DE. (a) The solid line represents a position of the unactivated wing while the dash line represents a new position of the activated wing. (b) Effect drawing of the bionics aerocraft with hinge flapping wings.

mimicking biological movements, making it essential to model the dynamic performance of the configuration. In theoretical studies, models characterizing the nonlinear dynamics of DEs are already established. Zhu *et al.* studied the nonlinear oscillations of a DE balloon around an equilibrium state and subsequently analyzed the resonance behavior of a DE membrane pre-stretched and mounted on a rigid circular ring under parametric excitation.[20,21] Li *et al.* studied the dynamics of a tunable DE resonator and identified the safe range for failure prevention when actuating the resonator.[15] Conclusions of these models coincide well with experimental observations for each specific actuator. Meanwhile, no study focused on the dynamics of DE during the actuation of a hinge configuration. To master the performance and guide the design of the configuration in dynamic field, establishing a theoretical model is obligatory.

To study the static and dynamic performance of the hinge configuration actuated by DE actuators, we analyze the deformation and vibration of DE actuation. First, we present the mechanism of a hinge configuration with integrated DEs and deduce the kinetic equation using the method of variational and force analysis. Second, we describe the state of equilibrium under static voltage when DE undergoes two modes of deformation: "uniaxial deformation" and "pure shear." The configuration shows a small and unstable rotary angle when DE undergoes "uniaxial deformation." In contrast, the structure of DE undergoing "pure shear" exhibits a good and stable mechanical behavior and the computational results fit well with the experimental data from literature. In the following section, we study the configuration's small oscillation around a state of equilibrium and show that the natural frequency can be tuned by varying parameters. Subject to an alternating voltage excitation, the configuration shows resonance behavior at multiple frequencies. Our theoretical studies on static and dynamic performances of the configuration were concluded in the last section.

MODEL OF DE INTEGRATED HINGE CONFIGURATION

Mechanism in Hinge Configuration

One of the potential applications of DE integrated hinge configuration is working as an air-borne vehicle with flapping wing, as showed in Figure 1. Each hinge flapping wing consists of two parallel DE films pre-stretching each other by a hinged rigid frame. The layer number of DEs on each side is flexible depending on the required performance of the configuration. Referring to Figure 1(a), at the unactivated state, the wing is in the neutral position, represented by the solid line. When the driving voltage is applied to the lower side, the DE on this side expands while the upper DE shrinks due to elastic stress. Accordingly the wing rotates to a new position, denoted by the dash line. Similarly, activating the DE on the upper side will generate a reverse rotary motion. By activating the DE on either side alternatively, the flapping wing configuration performs a reciprocating swinging which is comparable to the motion of a real bird's wing.

Constitutive Equation of DE

Figure 2 illustrates the mechanical model of a dielectric elastomer film. In the undeformed state, the DE membrane has a rectangular shape with a thickness L_3 and length L_1 in one-direction and length L_2 in two-direction. Subject to forces P_1 and P_2, the membrane reduces its thickness and expands to a new dimensions L_1^p, L_2^p, and L_3^p. The pre-stretch extensional ratios are defined as $\lambda_1^p = L_1^p/L_1$, $\lambda_2^p = L_2^p/L_2$, and $\lambda_3^p = L_3^p/L_3$. Figure 2(c) shows the actuated state of a DE film with dimensions l_1, l_2, and l_3, when voltage Φ is applied. Similarly, we define the overall stretch ratios by $\lambda_1 = l_1/L_1$, $\lambda_2 = l_2/L_2$, and $\lambda_3 = l_3/L_3$. The DE here is assumed as an ideal dielectric elastomer whose density and dielectric constant are independent of deformation, therefore, we have $\lambda_3 = \lambda_1^{-1}\lambda_2^{-1}$. The amount of accumulated charges is $+Q$ and $-Q$ on each electrode in the actuated state can be formulated as:

$$Q = \Phi \frac{\varepsilon L_1 L_2}{L_3} \lambda_1^2 \lambda_2^2, \tag{1}$$

where ε is the permittivity.

Based on the nonlinear field theory of dielectric elastomer,[22–24] we define the DE film as a thermodynamic system with three independent variables λ_1, λ_2, and Φ. The thermodynamics of the dielectric elastomer is characterized by the density of Helmholtz free energy W, which is the function of the three independent variables $W(\lambda_1, \lambda_2, \Phi)$ and composed of an elastic energy density and a static electric energy density

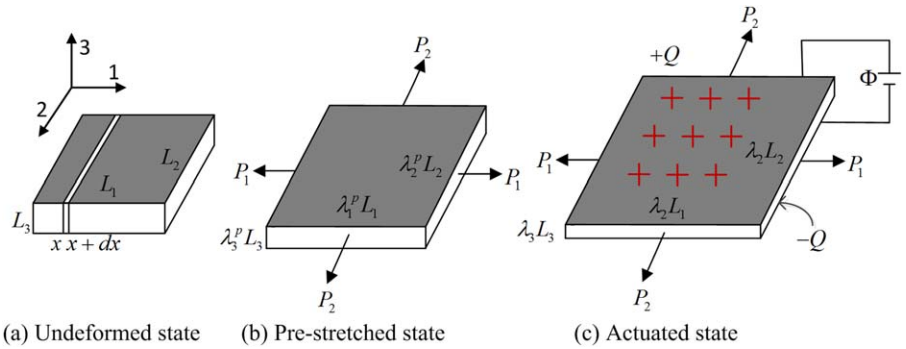

Figure 2. Schematics of a DE film in three states. (a) Undeformed state. A DE film under no electromechanical loads has dimensions $L_1 \times L_2 \times L_3$. (b) Pre-stretched state. Subject to only mechanical loads P_1 and P_2, DE attains dimensions $\lambda_1^p L_1 \times \lambda_2^p L_2 \times \lambda_3^p L_3$. (c) Actuated state. Subject to both electromechanical loads, P_1, P_2, and Φ, DE has dimensions $\lambda_1 L_1 \times \lambda_2 L_2 \times \lambda_3 L_3$. Because of incompressibility, we obtain $\lambda_3 = \lambda_1^{-1}\lambda_2^{-1}$. [Color figure can be viewed in the online issue, which is available at wileyonlinelibrary.com.]

$$W = \frac{1}{2}\mu\left(\lambda_1^2 + \lambda_2^2 + \lambda_1^{-2}\lambda_2^{-2} - 3\right) + \frac{\varepsilon\Phi^2}{2L_3^2}\lambda_1^2\lambda_2^2. \quad (2)$$

In eq. (2), the first term on the right hand side is the elastic energy density where μ is the shear modulus and the second term is the static electric energy density. Here, we use a Neo-Hookean model to calculate the elastic energy density.

Under the constant electromechanical loads P_1, P_2, and Φ, the DE film attains a state of equilibrium. When the dimension varies by δl_1 and δl_2, the mechanical loads P_1 and P_2 do work of $P_1\delta l_1$ and $P_2\delta l_2$. When the charge on the electrodes varies by δQ, the applied voltage Φ does work of $\Phi\delta Q$. As showed in Figure 2(a), the inertial force in each material element during actuation along one-direction is $-\rho L_2 L_3 dx(d^2x\lambda_1/dt^2)$. The virtual work done by the material element is $-\rho L_2 L_3 dx(d^2x\lambda_1/dt^2)\delta x\lambda_1$. The total virtual work done by the inertial force can be obtained by integrating x along the one-direction

$\int_0^{L_1} -\rho L_2 L_3 dx(d^2x\lambda_1/dt^2)\delta x\lambda_1 = -\frac{1}{3}\rho L_1^3 L_2 L_3 \delta\lambda_1(d^2\lambda_1/dt^2)$, where ρ is the density of DE, which is independent of the deformation.

For an arbitrary variation of the thermodynamic system, the variation of the total free energy equals the work done by the mechanical loads, the voltage, and the inertial force, namely

$$L_1 L_2 L_3 \delta W = P_1\delta L_1\lambda_1 + P_2\delta L_2\lambda_2 + \Phi\delta Q - \frac{1}{3}\rho L_1^3 L_2 L_3 \frac{d^2\lambda_1}{dt^2}\delta\lambda_1. \quad (3)$$

Inserting eqs. (1) and (2) into eq. (3), and reviewing that the DE film is a thermodynamic system with three variables λ_1, λ_2, and Φ, we obtain the electromechanical coupling constitutive equation as follows,

$$S_1 = \frac{1}{3}\rho L_1^2\frac{d^2\lambda_1}{dt^2} + \mu\lambda_1 - \mu\lambda_1^{-3}\lambda_2^{-2} - \frac{\varepsilon\Phi^2}{L_3^2}\lambda_1\lambda_2^2 \quad (4)$$

$$S_2 = \mu\lambda_2 - \mu\lambda_1^{-2}\lambda_2^{-3} - \frac{\varepsilon\Phi^2}{L_3^2}\lambda_1^2\lambda_2, \quad (5)$$

where S_1 and S_2 are nominal stresses defined by $S_1 = P_1/(L_2L_3)$ and $S_2 = P_2/(L_1L_3)$.

Kinetic Equation of the Hinge Configuration

If the DE films on both sides of the hinge structure have the same pre-stretch ratios and layer numbers, the configuration will hold in the neutral position initially, as showed in Figure 3(a). When DE on one side is subject to a voltage and expands, the DE on the other side will shrink due to the elastic stress. Subsequently the hinge rotates to a new position, Figure 3(b). Suppose the hinge obtains a rotary angle θ when activating one side's DE, we can deduce the kinetic equation as following by force analysis,

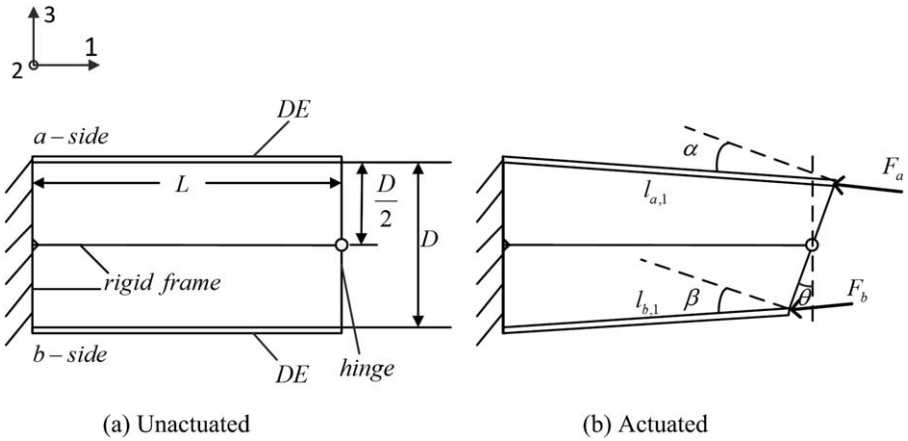

Figure 3. Schematics of active hinge configuration in two states. (a) Unactuated state. When DEs are subject to no voltage, the hinge configuration is in the neutral position. (b) Actuated state. The configuration rotates to a certain position when voltage is applied to DEs on one side.

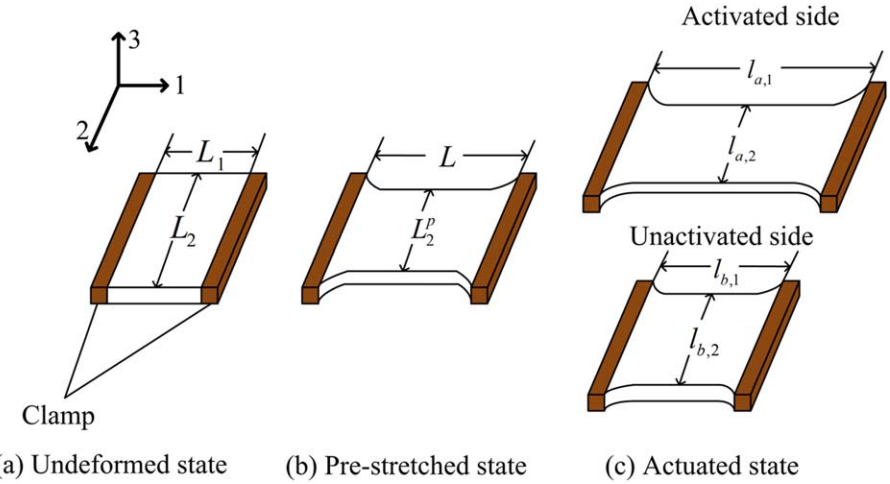

Figure 4. Schematics of DE with uniaxial force in three states. (a) Undeformed state. Two edges of a DE film without electromechanical loads are fixed by clamps. (b) Pre-stretched state. The film is pre-stretched along one-direction, consequently causing a shrinkage in two-direction. (c) Actuated state. The activated side DE elongates in one-direction while the unactivated side DE shrinks in one-direction. [Color figure can be viewed in the online issue, which is available at wileyonlinelibrary.com.]

$$F_a \cos\alpha \frac{D}{2} - F_b \cos\beta \frac{D}{2} + J\frac{d^2\theta}{dt^2} = 0, \tag{6}$$

where J and θ refer to the rotational inertia and the rotary angle of the hinge, respectively. α and β are functions of θ obtained by geometrical accommodation, see Appendix A. F_a and F_b are acting forces on the hinge caused by the DE films on both sides. D and L are structural parameters marked in Figure 3.

Based on eq. (4), we get the formulations of F_a and F_b,

$$F_{a,1} = nL_2L_3\left(\frac{1}{3}\rho L_1\frac{d^2 l_{a,1}}{dt^2} + \mu\lambda_{a,1} - \mu\lambda_{a,1}^{-3}\lambda_{a,2}^{-2} - \frac{\varepsilon\Phi^2}{L_3^2}\lambda_{a,1}\lambda_{a,2}^2\right) \tag{7}$$

$$F_{b,1} = nL_2L_3\left(\frac{1}{3}\rho L_1\frac{d^2 l_{b,1}}{dt^2} + \mu\lambda_{b,1} - \mu\lambda_{b,1}^{-3}\lambda_{b,2}^{-2}\right), \tag{8}$$

where n represents the number of layers of pre-stretched DE films.

Recalling that the final mechanical output is the hinge's rotary angle θ, we regard $l_{a,1}$, $l_{b,1}$, $\lambda_{a,1}$, $\lambda_{a,2}$, $\lambda_{b,1}$, and $\lambda_{b,2}$ as intermediate variables. $l_{a,1}$, $l_{b,1}$, $\lambda_{a,1}$, and $\lambda_{b,1}$ can be written as functions of θ. The detailed derivation is available in Appendix A. Expressions of $\lambda_{a,2}$ and $\lambda_{b,2}$ depend on the DE's deformation mode. By inserting eqs. (7) and (8) into eq. (6) and reducing, the kinetic equation takes the form as following,

$$\frac{d^2\theta}{dt^2} + \Delta\left(\frac{d\theta}{dt}\right)^2 + \varphi\left(\theta, \lambda_{a,1}, \lambda_{a,2}, \lambda_{b,1}, \lambda_{b,2}, \Phi\right) = 0, \tag{9}$$

where $\Delta = \frac{C_1\cos\alpha - C_3\cos\beta}{C_2\cos\alpha - C_4\cos\beta + \frac{6J}{n\rho DL_1L_2L_3}}$ and

$$\varphi\left(\theta, \lambda_{a,1}, \lambda_{a,2}, \lambda_{b,1}, \lambda_{b,2}, \Phi\right) = \frac{\left(\mu\lambda_{a,1} - \mu\lambda_{a,1}^{-3}\lambda_{a,2}^{-2} - \frac{\varepsilon\Phi^2}{L_3^2}\lambda_{a,1}\lambda_{a,2}^2\right)\cos\alpha - \left(\mu\lambda_{b,1} - \mu\lambda_{b,1}^{-3}\lambda_{b,2}^{-2}\right)\cos\beta}{\frac{1}{3}\rho L_1(C_2\cos\alpha - C_4\cos\beta) + \frac{2J}{nDL_2L_3}}.$$

In order to get the differential equation about θ, the second derivative of $l_{a,1}$ and $l_{b,1}$ in eqs. (7) and (8) must be written as formulas composed of the first and the second derivative of θ, where $C_i (i = 1, \ldots, 4)$ represents the related coefficient of the derivative of θ. The detailed signification and derivation of symbols C_1, C_2, C_3, and C_4 are shown in Appendix B. The hinge's kinetic equation is a nonlinear second order ordinary differential equation involving a quadratic dependence on the first derivative of the rotary angle. All the following analyses are based on solving eq. (9) with software MATLAB.

ANALYSIS OF STATIC PERFORMANCE

When the DE on one side is subject to a constant voltage Φ, the configuration will rotate to a new state of equilibrium. This state of equilibrium is described by the hinge's rotary angle θ_{eq} independent of time. With respect to eq. (9), the first and second derivative of θ vanish when the configuration is at a static state. Thus, we obtain the governing equation at the state of equilibrium as follows,

$$\varphi\left(\theta, \lambda_{a,1}, \lambda_{a,2}, \lambda_{b,1}, \lambda_{b,2}, \Phi\right) = 0. \tag{10}$$

Note that the static rotary angle θ_{eq} is independent of the DE's dimension in the two-direction and the number of layers of the pre-stretched DE films.

In the following computational simulation, we use a hinge configuration with $L = 0.05\,m$ and $D = W = 0.03\,m$. VHB4910 is selected as the dielectric elastomer for its excellent actuating performance. The parameters of the DE used are $L_3 = 1$ mm, $\rho = 1.2\,\mathrm{kg}\times\mathrm{m}^{-3}$, $\varepsilon = 3.9\times10^{-11}$ F/m, and $\mu = 60$ kPa.[18,25] Though the permittivity ε is dependent on temperature, pre-stretch, frequency and electrode materials, the change is small in the case of small deformation and low frequency.[26–28] In this article, we regard the permittivity as constant considering the largest aspect pre-stretch ratio is 9 and the frequency is less than 600 Hz, at ambient temperature.

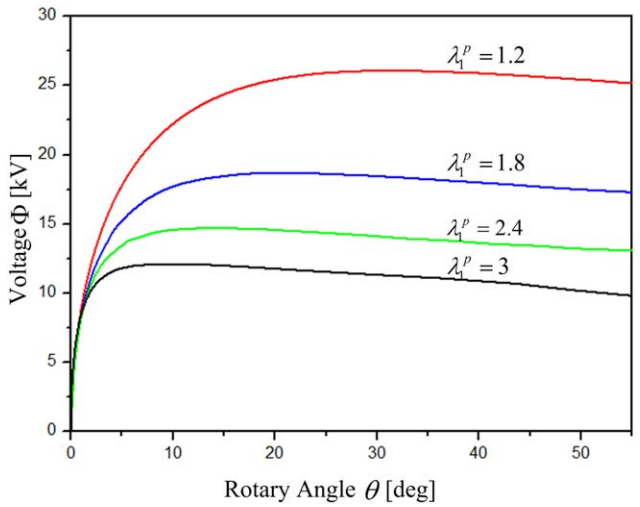

Figure 5. Rotary angle of the configuration is plotted when DE undergoes uniaxial deformation at several levels of λ_1^p. All the curves show non-monotonic changes with one voltage peak value. [Color figure can be viewed in the online issue, which is available at wileyonlinelibrary.com.]

The dielectric elastomer shows different electromechanical deformations depending on the loading and constraint conditions. This has been proven theoretically and experimentally by Lu *et al.* and Huang *et al.*[29,30] In the current hinge configuration, the DE is activated in two deformation modes: uniaxial and pure shear deformation. Either mode shows a special property in electromechanical coupling and will be studied and compared in the following sections.

DE with Uniaxial Force

Figure 4 shows the uniaxial deformation of the DE. In this case, the force in one-direction gives rise to a shrinkage of the DE in two-direction, consequently the nominal stress S_2 keeps zero basically. For the actuated DE(a-side), eq. (5) reduces to

$$\lambda_{a,2} = \left(\lambda_{a,1}^2 - \frac{\varepsilon \Phi_a{}^2}{\mu L_3^2}\lambda_{a,1}^4\right)^{-\frac{1}{4}}. \quad (11)$$

Similarly, for the unactuated DE (b-side), eq. (5) reduces to

$$\lambda_{b,2} = \frac{1}{\sqrt{\lambda_{b,1}}}. \quad (12)$$

These two equations describe the relation between λ_1 and λ_2 when the DE is subject to a uniaxial force.

Inserting eqs. (11) and (12) combined with eqs. (A6) and (A7) into eq. (10), we obtain $\varphi\left(\theta_{\text{eq}}, \lambda_1^p, \Phi\right) = 0$.

Curves in Figure 5 describe the relation between the rotary angle and the applied voltage at several levels of pre-stretch ratios in one-direction. With the increase of voltage, the rotary angle increases slowly until the voltage reaches its maximum value. The maximum voltage value represents a critical state. Below the critical voltage, each voltage corresponds to two values of rotary angle. The lower value of rotary angle on the rising part of the curve corresponds to the stable state while the one on the decreasing part refers to the unstable state. At the maximum value of voltage, the rotary angle may increase quickly due to the rapid thinning of the DE under a small perturbation, so that the voltage induces a high electric field. The positive feedback may cause a drastic thinning of DE until electric breakdown. This phenomenon is well known as the electromechanical instability (EMI) as explained by Zhao and Suo.[22,23]

Another interesting phenomenon is that enlarging the pre-stretch ratio along one-direction lowers the critical voltage and decreases the accessible rotary angle correspondingly. Upon pre-stretch the membrane stiffens in one-direction but remains soft in two-direction. This anisotropy in elasticity causes the DE to deform mainly in two-direction and thin drastically.[29] This explains the small rotary angle when the DE is subject to uniaxial force.

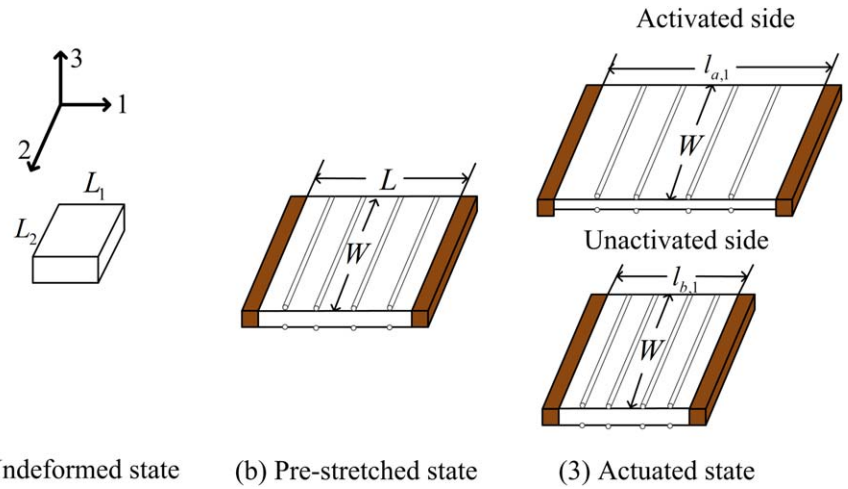

Figure 6. Schematics of DE undergoing pure-shear deformation in three states. (a) Undeformed state. The film is not stretched with dimensions $L_1 \times L_2$. (b) Pre-stretched state. The film is pre-stretched to dimensions $L \times W$ and stiff fibers are added to constrain the shrinkage in two-direction. (c) Actuated state. For DEs on both two sides, dimensions in one-direction change while dimensions in two-direction keep as W during the actuation. [Color figure can be viewed in the online issue, which is available at wileyonlinelibrary.com.]

Pure Shear Deformation

As DE undergoes uniaxial deformation suffering from EMI, various methods are adopted to realize the pure shear deformation of DE.[13,29,30] In Figure 6, both DEs are constrained by the stiff fiber effectively and they undergo pure shear deformation. The stretch ratios in two-direction follows,

$$\lambda_{a,2}=\lambda_{b,2}=\lambda_2^p. \tag{13}$$

Inserting eqs. (13), (A6), (A7), and (A8) into eq. (10), we formulate the governing equation at a state of equilibrium $\varphi\left(\theta_{eq},\lambda_1^p,\lambda_2^p,\Phi\right)=0$. This equation indicates the final rotary angle, which is determined by the pre-stretch ratios λ_1^p and λ_2^p under a given voltage.

Figure 7(a) plots the rotary angle–voltage curves of equilibrium state of DE in pure shear deformation compared with the DE in uniaxial deformation, at the same pre-stretch ratio $\lambda_1^p=3$.

The pure-shear deformation denoted by the blue line shows a monotonic change while the uniaxial deformation denoted by the red line has a peak value. As is shown by the blue line, with the voltage increasing, the rotary angle increases monotonically, which means the electromechanical instability is avoided. At the same voltage, the configuration of the DE in pure shear shows a larger rotary angle than that in uniaxial elongation.

Figure 7(b,c) plots the curves of rotary angle versus voltage in pure shear deformation. When the DE is equally biaxial pre-stretched, the rotary angle increases with the pre-stretch ratio enlarging. This can be easily understood as larger area pre-stretch ratio makes the DE thinner, accordingly inducing a higher electric field and Maxwell stress,[4] considering a condition that DEs have the same area pre-stretch ratio as $\lambda_1^p\times\lambda_2^p=9$. As is shown in Figure 7(c), a DE with a lower level of λ_1^p shows better actuating performance. The unequal biaxial pre-stretch induces anisotropy, so that DE deforms mainly in the less pre-stretch direction, which has a lower stiffness. However, Li *et al.* has verified that the DE may fail in the less pre-stretch direction due to the compliance of the materials.[31] Therefore, the unequal biaxial pre-stretch enhances the actuating performance but lowers the stability of the DE compared to equal biaxial pre-stretch.

We compare the computational results with the experimental data extracted from Ref [18] Jordi *et al.* manufactured the active hinge configuration with $L=0.05$ m and $W=0.03$ m. VHB4910 is selected with a pre-stretch ratio $\lambda_1\times\lambda_2=3\times5$. The parameters used in the calculation are the same as those in the experiment. As depicted in Figure 8, the computational results denoted by the blue line fit well with the experimental results denoted by the red dots. A small difference is observed. The theoretical calculation overestimates the experimental results. With the voltage increasing, the discrepancy becomes smaller. This is understood as we adopt an ideal model which does not take into account the friction at the revolute and the efficiency of the fiber constraint.

Comparing the above two modes of DE's deformation, pure shear deformation is identified to be both stable and efficient, thus the dynamic analyses of the configuration are based on this mode of deformation.

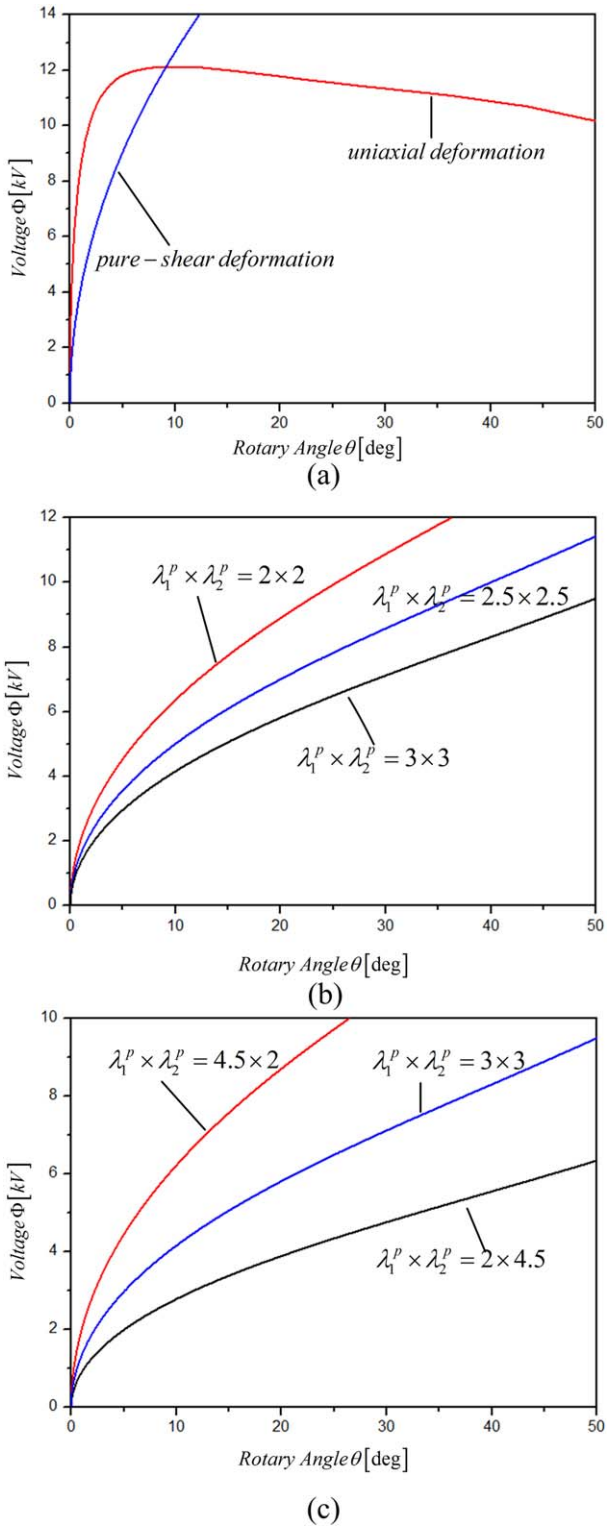

Figure 7. Rotary angle of the configuration is plotted when DE undergoes different modes of deformation. (a) Curves of actuation when DE undergoes uniaxial and pure shear deformation with the same $\lambda_1^p=3$. (b) Curves of actuation when DE undergoes pure shear deformation with different equal-biaxial pre-stretch ratios. (c) Curves of actuation when DE undergoes pure-shear deformation with the same area pre-stretch ratio. [Color figure can be viewed in the online issue, which is available at wileyonlinelibrary.com.]

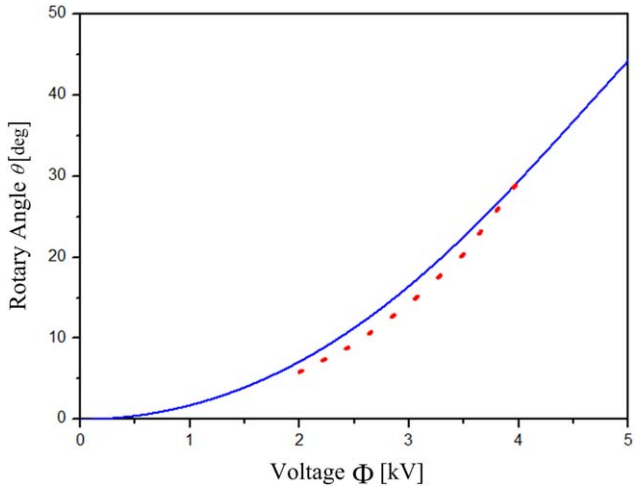

Figure 8. Comparison between experimental data represented by red dots and computational results represented by the blue solid line. [Color figure can be viewed in the online issue, which is available at wileyonlinelibrary.com.]

ANALYSIS OF DYNAMIC PERFORMANCE

We use the nonlinear vibration modeling to analyze the oscillation of the hinge configuration.[15,20,21] Subject to a static voltage, the hinge configuration deforms to a state of equilibrium with a rotary angle θ_{eq}. This structure can oscillate around the equilibrium state under a small perturbation. Subsequently, the rotary angle turns to be $\theta(t)=\theta_{eq}+\delta(t)$. Here, $\delta(t)$ is the amplitude of the perturbation and thought to be very small. We expand θ as a power series in $\delta(t)$ around the equilibrium state rotary angle θ_{eq}. To the first order in $\delta(t)$, the motion eq. (9) becomes

$$\frac{d^2\delta}{dt^2}+\Delta\left(\frac{d\delta}{dt}\right)^2+\delta\frac{d\varphi(\theta_{eq},\lambda_1^p,\lambda_2^p,\Phi,n,J)}{d\theta}=0. \quad (14)$$

The natural frequency takes form as,

$$\omega_0^2=\frac{d\varphi(\theta_{eq},\lambda_1^P,\lambda_2^P,\Phi,n,J)}{d\theta}. \quad (15)$$

The natural frequency of the hinge configuration ω_0 is determined by the following parameters: static voltage Φ, pre-stretch ratios in two directions λ_1^p and λ_2^p, the layer number of DE films n, and the rotational inertia of the hinge J. ω_0 can be calculated by adopting the following method: first we obtain the rotary angle θ_{eq} by solving eq. (10) under a given set of parameters; inserting θ_{eq} and the corresponding parameters into eq. (15), the natural frequency ω_0 is then obtained. Because of the nonlinearity in material and coupling, the natural frequency of the structure is highly tunable.

To investigate the effects of given parameters on the natural frequency, we first present a set of initial values as $\{\Phi=2000\text{V}, \lambda_1^p=3, \lambda_2^p=3, n=1, J=2\times10^{-7}\,\text{kg}\times\text{m}^2\}$. We separate one parameter from others for an individual study while the others keep constant as the presented values. Figure 9(a–e) describes the relations between the natural frequency and the parameters affecting it. As shown in Figure 9(a), with J increasing, ω_0 decreases from about 350 to 220 Hz. In contrast, adding the number of DE films induces a big increment of ω_0. This can be easily understood as enlarging J means the increment of passive mass, accordingly reducing ω_0 drastically. Suppose a limiting case where J is big enough that the DE's actuating capability almost has no effect, thus ω_0 reduces to almost zero. However, adding more layers of DE films weakens the effect of hinge's rotational inertia. When the number of DE films is large enough, the hinge's rotational inertia can be neglected and ω_0 is almost equal to DE's natural frequency of this structure.

Natural frequency versus voltage curve plotted in Figure 9(c) shows a non-monotonic variation trend. With the increasing of voltage, the natural frequency first falls slightly and then increases rapidly. At a lower level of voltage, the compressive Maxwell stress softens the membrane and reducing its ω_0. The rising part of the curve reflects the stiffening of the configuration at a higher voltage.[15,32] Figure 9(d,e) plots the pre-stretch versus natural frequency. When λ_2^p and Φ are set as the presented values, ω_0 enhances with the enlarging of λ_1^p. Owing to the lower level of voltage $\Phi=2000\,\text{V}$, the pre-stress due to λ_1^p dominates over the Maxwell stress, which strengthens the DE and subsequently enhances ω_0. In Figure 9(e), ω_0 shows a decreasing trend with the enlargement of λ_2^p. In pure shear deformation mode, unequal biaxial pre-stretch induces anisotropy on the DE. The less pre-stretched direction is comparatively compliant, accordingly suppressing the ω_0.

The dynamics of the hinge configuration can be very complicated when the voltage varies with time. Based on the previous work done by Li *et al.* and Zhu *et al.*,[15,20,21] we investigate the intricate dynamic behavior of the configuration. We prescribe the applied voltage on the a-side as:

$$\Phi(t)=\Phi_{dc}+\Phi_{ac}\sin(\Omega t), \quad (16)$$

where Φ_{dc}, Φ_{ac}, and Ω indicate the DC voltage, the amplitude of the AC voltage, and the excitation frequency, respectively. Inserting eq. (13) into eq. (7) and reducing,

$$\frac{d^2\theta}{dt^2}+\Delta\left(\frac{d\theta}{dt}\right)^2+\frac{\left(\mu\lambda_{a,1}-\mu\lambda_{a,1}^{-3}\lambda_{a,2}^{-2}-\frac{\varepsilon\Phi_{dc}^2}{L_3^2}\left(1+\frac{\Phi_{ac}}{\Phi_{dc}}\sin(\Omega t)\right)^2\lambda_{a,1}\lambda_{a,2}^2\right)\cos\alpha-\left(\mu\lambda_{b,1}-\mu\lambda_{b,1}^{-3}\lambda_{b,2}^{-2}\right)\cos\beta}{\frac{1}{3}\rho L_1(C_2\cos\alpha-C_4\cos\beta)+\frac{2J}{nDL_2L_3}}=0. \quad (17)$$

Subject to an oscillatory voltage, the active hinge configuration will vibrate, which is described by the time-dependent rotary angle θ obtained for given initial condition. Note that in this numerical simulation, except for the voltage, the other parameters are prescribed as initial values presented above. First, we apply a constant voltage as 2000 V, the configuration rotates to a new position with $\theta_{eq}=0.0392$. Then we apply the oscillatory voltage with $\Phi_{dc}=2000\,\text{V}$, $\Phi_{ac}=200\,\text{V}$, and a specific value of Ω.

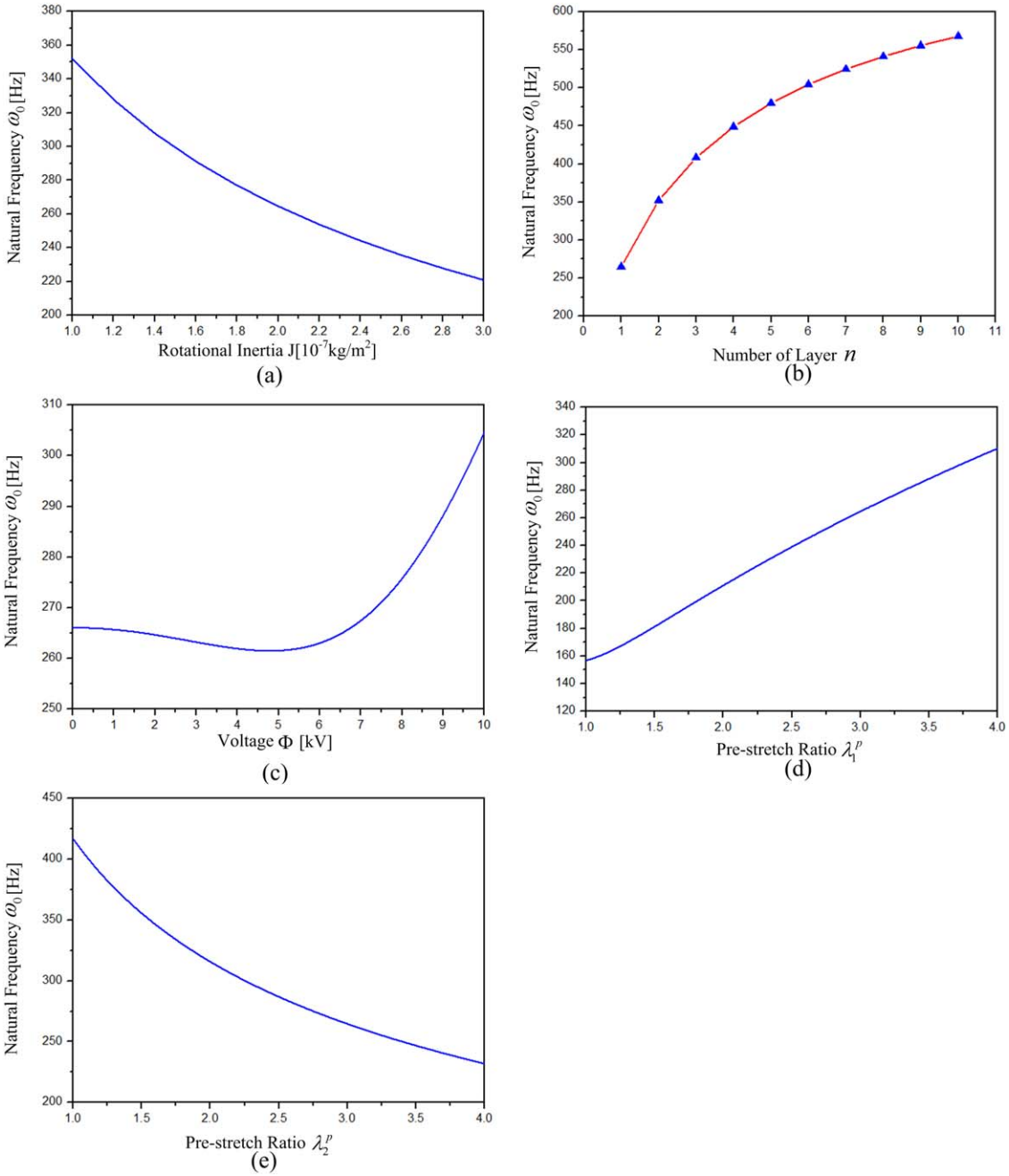

Figure 9. The natural frequency of the configuration is plotted as a function of the corresponding parameters. The natural frequencies show monotonic changes with the varying of rotational inertia (a), number of layer (b), pre-stretch ratio λ_1^p (d), and λ_2^p (e). As is shown in (c), with the increase of voltage, the natural frequency increases quickly after a slight decreasing. [Color figure can be viewed in the online issue, which is available at wileyonlinelibrary.com.]

When $\theta(t)$ attains a steady oscillation, we define the amplitude of oscillation as half of the difference between the maximal and minimal values.

Figure 10 plots the amplitude of oscillation in the frequency domain. At the frequency of 278 Hz, the amplitude of oscillation reaches its maximum value. This phenomenon is well known as harmonic resonance. The superharmonic resonance is also predicted: the configuration also resonates when the excitation frequency approaches half of the natural frequency. By varying the DC voltage Φ_{dc}, the natural frequency can be tuned which has been discussed above.

CONCLUSION

In this article, we established the kinetic equation of an active hinge configuration actuated by DE. Subject to a constant voltage, the hinge can rotate to an equilibrium state and the state is

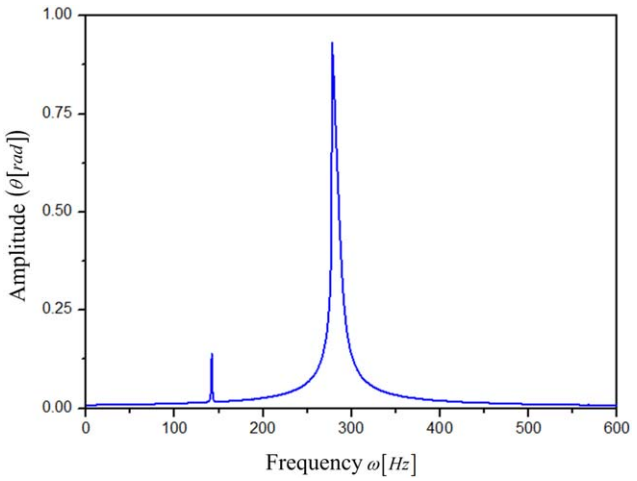

Figure 10. Subject to a sinusoidal voltage, the configuration resonates at two frequencies of excitation, known as the superharmonic and harmonic resonance. The harmonic resonance frequency is about twice as large as the superharmonic resonance frequency. [Color figure can be viewed in the online issue, which is available at wileyonlinelibrary.com.]

affected by the modes of deformation and pre-stretch ratios of the DE. We theoretically study the effects of above parameters on the configuration, which shows that DE undergoing pure shear deformation has a larger actuating capacity without an electromechanical instability compared to uniaxial deformation. Our theoretical predictions are verified by the static experiments conducted by Jordi. Under a small perturbation, the configuration may oscillate around the equilibrium state. The natural frequency of the configuration can be tuned by changing the pre-stretch ratios, number of layer, applied voltage, and the rotational inertia of the hinge. When the applied sinusoidal voltage varies continuously, the configuration resonates at two frequencies during excitation, known as harmonic and superharmonic resonance. However, dynamic experiments of the configuration are expected for further investigation. In addition, effects of viscoelasticity on the static and dynamic characteristics should also be considered, because they affect the electromechanical coupling efficiency.[33,34] Our following work will involve the above two aspects.

APPENDIX A: DERIVATION OF CORRESPONDING INTERMEDIATE VARIABLES

Referring to Figure 3(b), adopting cosine theorem, we can obtain functions $\boldsymbol{l_{a,1}}(\theta)$ and $\boldsymbol{l_{b,1}}(\theta)$ as below,

$$l_{a,1}=\left(L^2+\frac{D^2}{2}-D\sqrt{L^2+\frac{D^2}{4}}\cos\left(\theta+\arctan\frac{2L}{D}\right)\right)^{0.5} \tag{A1}$$

$$l_{b,1}=\left(L^2+\frac{D^2}{2}-D\sqrt{L^2+\frac{D^2}{4}}\cos\left(\arctan\frac{2L}{D}-\theta\right)\right)^{0.5}. \tag{A2}$$

In the upper equations, L and D are dimensions of the rigid structure labeled in Figure 3(a). Note that L is equal to the length of pre-stretched DE in one-direction, $L^p_{a,1}$ and $L^p_{b,1}$.
Similarly using sine theorem, we obtain the relation between α, β, and θ.

$$\cos\alpha=\frac{\sqrt{L^2+\frac{D^2}{4}}\sin\left(\theta+\arctan\frac{2L}{D}\right)}{l_{a,1}} \tag{A3}$$

$$\cos\beta=\frac{\sqrt{L^2+\frac{D^2}{4}}\sin\left(\arctan\frac{2L}{D}-\theta\right)}{l_{b,1}}. \tag{A4}$$

The final stretch ratio of DE along the two directions can be formulated as a function of the pre-stretch ratio in the two directions λ_1^p, λ_2^p, and the rotary angle θ.

$$\lambda_1^p=\frac{L_1^p}{L_1}=\frac{L}{L_1} \tag{A5}$$

$$\lambda_{a,1}=\frac{l_{a,1}}{L_1}=\frac{L_1^p}{L_1}\frac{l_{a,1}}{L_1^p}=\lambda_1^p\frac{l_{a,1}}{L} \tag{A6}$$

$$\lambda_{b,1}=\frac{l_{b,1}}{L_1}=\frac{L_1^p}{L_1}\frac{l_{b,1}}{L_1^p}=\lambda_1^p\frac{l_{b,1}}{L}. \tag{A7}$$

Especially in the condition of DE's pure shear deformation, we can deduce

$$\lambda_2^p=\frac{L_2^p}{L_2}=\frac{W}{L_2}, \tag{A8}$$

where W refers to the width of the configuration.

APPENDIX B: DEFINITION AND DERIVATION OF SYMBOLS

Note that the final mechanical output is the hinge's rotary angle θ. Based on the previous work in APPENDIX A, combined with derivation rules for compound function, we can translate the second derivative of $l_{a,1}$ and $l_{b,1}$ into a formula composed of the first and the second derivative of θ.

$$\frac{dl}{dt}=\frac{dl}{d\theta}\frac{d\theta}{dt}$$
$$\frac{d^2l}{dt^2}=\frac{d}{dt}\left(\frac{dl}{d\theta}\frac{d\theta}{dt}\right)=\frac{d^2l}{d\theta^2}\left(\frac{d\theta}{dt}\right)^2+\frac{dl}{d\theta}\frac{d^2\theta}{dt^2}. \tag{B1}$$

Inserting eqs. (A1) and (A2) into eq. (B1),

$$\frac{d^2l_{a,1}}{dt^2}=C_1\left(\frac{d\theta}{dt}\right)^2+C_2\frac{d^2\theta}{dt^2} \tag{B2}$$

$$\frac{d^2l_{b,1}}{dt^2}=C_3\left(\frac{d\theta}{dt}\right)^2+C_4\frac{d^2\theta}{dt^2}, \tag{B3}$$

where $C_i(i=1,\cdots,4)$ represents $d^2l_{a,1}/d\theta^2$, $dl_{a,1}/d\theta$, $d^2l_{b,1}/d\theta^2$, and $dl_{b,1}/d\theta$, respectively.

ACKNOWLEDGMENTS

This research is supported by the National Natural Science Foundation of China (Grant No. 51290294). The authors gratefully acknowledge the support.

REFERENCES

1. Carpi, F.; Rossi, D. D.; Kornbluh, R.; Pelrineand, R.; Sommer-Larsen, P. Dielectric elastomers as electromechanical transducers: Fundamentals, Materials, Devices, Models

and Applications of an Emerging Electroactive Polymer Technology. Elsevier Science, **2008**; Chapter 11, pp 118–120.

2. Brochuand, P.; Pei, Q. *Macromol. Rapid Commun.* **2010**, *31*, 10.
3. Kofod, G.; Sommer-Larsen, P.; Kornbluhand, R.; Pelrine, R. *J. Intell. Mater. Syst. Struct.* **2003**, *14*, 787.
4. Pelrine, R.; Kornbluh, R.; Peiand, Q.; Joseph, J. *Science* **2000**, *287*, 836.
5. Choi, H. R.; Jung, K.; Ryew, S.; Nam, J.-D.; Jeon, J.; Kooand, J. C.; Tanie, K. *IEEE/ASME Trans. Mechatron.* **2005**, *10*, 581.
6. Carpi, F.; Frediani, G.; Turcoand, S.; De Rossi, D. *Adv. Funct. Mater.* **2011**, *21*, 4152.
7. Shian, S.; Dieboldand, R. M.; Clarke, D. R. *Opt. Express* **2013**, *21*, 8669.
8. McKay, T.; O'Brien, B.; Caliusand, E.; Anderson, I. *Appl. Phys. Lett.* **2010**, *97*, 062911.
9. Zhang, R.; Lochmatter, P.; Kunzand, A.; Kovacs, G. Smart Structures and Materials, **2006**, pp 61681T–61681T–61612.
10. Pei, Q.; Rosenthal, M.; Stanford, S.; Prahladand, H.; Pelrine, R. *Smart Mater. Struct.* **2004**, *13*, N86.
11. Lau, G.-K.; Lim, H.-T.; Teoand, J.-Y.; Chin, Y.-W. *Smart Mater. Struct.* **2014**, *23*, 025021.
12. Biggsand, S. J.; Hitchcock, R. N. SPIE Smart Structures and Materials+ Nondestructive Evaluation and Health Monitoring, **2010**, pp 76420I–76420I–76412.
13. Jordi, C.; Michel, S.; Kovacsand, G.; Ermanni, P. *Sens. Actuators A: Phys.* **2010**, *161*, 182.
14. Lochmatter, P.; Kovacsand, G.; Ermanni, P. *Smart Mater. Struct.* **2007**, *16*, 1415.
15. Li, T.; Quand, S.; Yang, W. *Int. J. Solids Struct.* **2012**, *49*, 3754.
16. Michel, S.; Dürager, C.; Zobeland, M.; Fink, E. The 14th International Symposium on: Smart Structures and Materials & Nondestructive Evaluation and Health Monitoring, **2007**, pp 65241Q–65241Q–65211.
17. Lochmatterand, P.; Kovacs, G. *Sens. Actuators A: Phys.* **2008**, *141*, 577.
18. Jordi, C.; Schmidt, A.; Kovacs, G.; Micheland, S.; Ermanni, P. *Smart Mater. Struct.* **2011**, *20*, 075003.
19. Jordi, C.; Micheland, S.; Fink, E. *Bioinspir. Biomim.* **2010**, *5*, 026007.
20. Zhu, J.; Caiand, S.; Suo, Z. *Polym. Int.* **2010**, *59*, 378.
21. Zhu, J.; Caiand, S.; Suo, Z. *Int. J. Solids Struct.* **2010**, *47*, 3254.
22. Zhao, X.; Suo, Z. *Appl. Phys. Lett.* **2007**, *91*, 061921.
23. Zhao, X.; Hongand, W.; Suo, Z. *Phys. Rev. B* **2007**, *76*, 134113.
24. Suo, Z. *Acta Mech. Sol. Sin.* **2010**, *23*, 549.
25. Xu, B.-X.; Mueller, R.; Theis, A.; Klassenand, M.; Gross, D. *Appl. Phys. Lett.* **2012**, *100*, 112903.
26. Jean-Mistral, C.; Sylvestre, A.; Basrourand, S.; Chaillout, J. *J. Smart Mater. Struct.* **2010**, *19*, 075019.
27. Sahu, R. K.; Pramanik, B.; Patra, K.; Bhaumik, S.; Pandeyand, A. K.; Setua, D. K. *J. Nanosci. Nanotechnol.* **2014**, *14*, 7439.
28. Qiang, J.; Chenand, H.; Li, B. *Smart Mater. Struct.* **2012**, *21*, 025006.
29. Lu, T.; Huang, J.; Jordi, C.; Kovacs, G.; Huang, R.; Clarkeand, D. R.; Suo, Z. *Soft Matter* **2012**, *8*, 6167.
30. Huang, J.; Lu, T.; Zhu, J.; Clarkeand, D. R.; Suo, Z. *Appl. Phys. Lett.* **2012**, *100*, 211901.
31. Li, B.; Chen, H.; Qiang, J.; Hu, S.; Zhuand, Z.; Wang, Y. *J. Phys. D: Appl. Phys.* **2011**, *44*, 155301.
32. Sheng, J.; Chen, H.; Liand, B.; Wang, Y. *Smart Mater. Struct.* **2014**, *23*, 045010.
33. Hong, W. *J. Mech. Phys. Sol.* **2011**, *59*, 637.
34. Zhao, X.; Kohand, S. J. A.; Suo, Z. *Int. J. Appl. Mech.* **2011**, *3*, 203.